



HAL
open science

Lone-pair self-containment in pyritohedron-shaped closed cavities: optimized hydrothermal synthesis, structure, magnetism and lattice thermal conductivity of $\text{Co}_{15}\text{F}_2(\text{TeO}_3)_{14}$

Minfeng Lü, Jianhua Jiang, Bei Zhu, Yuwei Zhao, Tianyu Zhu, Haoming Yang, Yong Jin, Houria Kabbour, Kwang-Yong Choi, William Harrison

► **To cite this version:**

Minfeng Lü, Jianhua Jiang, Bei Zhu, Yuwei Zhao, Tianyu Zhu, et al.. Lone-pair self-containment in pyritohedron-shaped closed cavities: optimized hydrothermal synthesis, structure, magnetism and lattice thermal conductivity of $\text{Co}_{15}\text{F}_2(\text{TeO}_3)_{14}$. Dalton Transactions, 2020, 49 (7), pp.2234-2243. 10.1039/c9dt04176a . hal-03059694

HAL Id: hal-03059694

<https://hal.science/hal-03059694>

Submitted on 14 Dec 2020

HAL is a multi-disciplinary open access archive for the deposit and dissemination of scientific research documents, whether they are published or not. The documents may come from teaching and research institutions in France or abroad, or from public or private research centers.

L'archive ouverte pluridisciplinaire **HAL**, est destinée au dépôt et à la diffusion de documents scientifiques de niveau recherche, publiés ou non, émanant des établissements d'enseignement et de recherche français ou étrangers, des laboratoires publics ou privés.

Lone-pair self-containment in pyritohedron-shaped closed cavities: Optimized hydrothermal synthesis, structure, magnetism and lattice thermal conductivity of $\text{Co}_{15}\text{F}_2(\text{TeO}_3)_{14}$

Minfeng Lü,^{a,*} ID Jianhua Jiang,^a Bei Zhu,^a Yuwei Zhao,^a Tianyu Zhu,^a Haoming Yang,^a Yong Jin,^a Houria Kabbour,^b Kwang-Yong Choi^c and William T. A. Harrison^d

^a School of Environmental & Chemical Engineering, Jiangsu University of Science and Technology, Zhenjiang 212003, Jiangsu, People's Republic of China

^b Univ. Lille, CNRS, Centrale Lille, ENSCL, Univ. Artois, UMR 8181 – UCCS – Unité de Catalyse et Chimie du Solide, F-59000 Lille, France

^c Department of Physics, Chung-Ang University, 84 Heukseok-ro, Dongjak-gu, Seoul 06974, Republic of Korea

^d Department of Chemistry, University of Aberdeen, Aberdeen, AB24 3UE, Scotland

Abstract

The new oxofluoride $\text{Co}_{15}\text{F}_2(\text{TeO}_3)_{14}$ has been prepared by optimized hydrothermal synthesis involving complex mineralization process. The crystal structure consists of a three-dimensional network of $\text{CoO}_5(\text{O},\text{F})$ octahedra, distorted CoO_5 square pyramids, TeO_3 trigonal pyramids and grossly distorted TeO_{3+3} octahedra, which are linked by sharing corners and edges. The Te(IV) lone pairs are accommodated within novel pyritohedron-shaped $[(\text{TeO}_3)_{14}]^{28-}$ units. This special framework provides a much larger free space that allows Te atoms to vibrate with large amplitude, which leads to extremely low lattice thermal conductivity. Magnetic susceptibility data for $\text{Co}_{15}\text{F}_2(\text{TeO}_3)_{14}$ show antiferromagnetic ordering below 9.6 K with a substantial orbital component to the effective magnetic moment. An $S=3/2$ honeycomblike spin network was carefully analyzed by experimental techniques and first principles calculation.

1. Introduction

Compounds with multiple anions (more than one anionic species), such as oxyhalides oxynitrides and oxyhydrides, have been attracted attention due to their diverse chemistries and structures that may lead to superior functionality.¹ Famous examples are the high- T_c

superconductors LaOFeAs² and Sr₂CuO₂F₂,³ the oxynitride semiconductors AMO₂N (A= Ba, Sr, Ca; M= Ta, Nb)⁴ and the oxyhydride BaTiO_{3-x}H_x,⁵ which exhibits hydride exchange and electronic conductivity. On another hand, the emergent mixed anion compounds have shown great potential for developing new thermoelectrics.^{6,7} Tellurites, however, possess rich and varied crystal chemistry because of the unpredictable and irregular coordination geometries adopted by the Te(IV) atoms, which can bond to between three and six O atoms. This behavior is characteristic of *p*-block cations with *ns*²*np*⁰ electronic configurations and may be ascribed to a second-order Jahn–Teller (SOJT) effect,^{8–10} which results in a stereochemically active lone pair of electrons^{11,12} that must be spatially accommodated within the crystal structure. In previous studies, it was found that the Te lone pairs can form one-dimensional lone-pair channels,¹³ where TeO_x (*x* = 3, 4, 5) polyhedra are connected to MO_y units (M = metal cation), or two-dimensional lone-pair sheets,¹⁴ whose interlayer spacing is large enough to accommodate other chemical species such as alkali metal cations.¹⁵ However, lone-pair ‘self-containments’, where extended tellurite topological networks are formed by themselves, are rare, with one example being the barium tellurites¹⁶ BaTe₃O₇ and BaTe₄O₉, which accommodate the Te^{IV} lone pairs in infinite, self-contained, one-dimensional tubes interspersed by the barium cations.

Recently, transition metal halo-tellurites and halo-selenites have been investigated as quantum spin systems with interesting magnetic and physical properties. For example, FeSeO₃F¹⁷ is composed of alternating antiferromagnetic chains, and FeTe₂O₅Br exhibits multiferroicity.¹⁸ These oxohalides can be divided into two categories: the larger halide ions (Cl[−] and Br[−]) with low coordination numbers act as terminal ligands, with examples being FeTe₂O₅X (X = Cl, Br),¹⁹ Cu₂Te₂O₅X₂,²⁰ Ni₅(TeO₃)₄X₂,¹⁴ Cu₄Te₅O₁₂Cl₄,²¹ and Fe₃Te₃O₁₀Cl.²² On the other hand, the smaller fluoride anion may act as a bridging species between transition metal cations in phases such as V₂Te₂O₇F₂,²³ MTeO₃F (M = Fe, Ga),²⁴ Co₂TeO₃F₂, and Co₂SeO₃F₂.²⁵ It may also be noted that different bonding preferences exist between the transition metal cation and the lone-pair cation. Transition metal cations prefer to bond with both oxygen and halide anions, while lone-pair cations prefer to exclusively coordinate to oxide anions.¹² This finding suggests that the crystal chemistry in transition metal halo-tellurite systems is governed not only by the asymmetric coordination of Te⁴⁺ cations but also by bonding preferences of the transition metal ions for oxide and halide anions to form M(O,X)_{*n*} polyhedra.

In this article, we extend multiple anions concept to transition metal halo-tellurites using the

optimized hydrothermal synthesis method, in contrast to previous studies that used unique mineralizers, *i.e.*, hydroxide, metal halide, and metal fluorides. Surprisingly, we found that the compound $\text{Co}_{15}\text{F}_2(\text{TeO}_3)_{14}$, **1**, features unique pyritohedron-shaped Te^{IV} lone-pair self-contained cavities, which exhibited extremely low lattice thermal conductivity (κ_{L}). Detailed structural and magnetic analyses are also presented.

2. Experimental section

A mixture of 0.015 mol (1.567 g) of RbF (Sigma-Aldrich, 99.8%), 1.50×10^{-4} mol (0.036 g) of $\text{CoCl}_2 \cdot 6\text{H}_2\text{O}$ (Energy Chemical, 99%) and 3.75×10^{-4} mol (0.060 g) of TeO_2 (Sigma-Aldrich, 99%) was placed in a Teflon-lined stainless steel autoclave (23 ml) with 0.016 ml of hydrazine monohydrate and 1.5 ml of deionized water. The vessel was sealed and heated to 220 °C for 72 hours and cooled slowly ($5 \text{ }^\circ\text{C h}^{-1}$) to room temperature. After filtering and rinsing with water, blue prismatic single crystals of **1** and polycrystalline metallic Te were recovered. Several attempts have been made to prepare **1** by solid-state reactions, but these attempts led to CoTeO_3 . It should be stressed that trace amounts of ammonium species are crucial to the formation of the $\text{Co}_{15}\text{F}_2(\text{TeO}_3)_{14}$ phase and should be optimized. $\text{Co}_2\text{Te}_3\text{O}_8$ was formed mainly upon addition of 0.008 ml of hydrazine monohydrate, while metallic Te was recovered upon addition of 0.024 ml of hydrazine monohydrate. Indeed, both alkali metal fluoride sources and ammonium species have been used as mineralizers to aid in the formation of the $\text{Co}_{15}\text{F}_2(\text{TeO}_3)_{14}$ phase, while ammonium species also play an important role to adjust pH. A single-phase polycrystalline sample of **1** was obtained by manually separating and grinding the single crystals (Figure S1). The cell parameters refined against the X-ray powder diffraction pattern [$a = 11.7067$ (5) Å, $c = 27.301$ (1) Å] are in good agreement with those obtained from the single crystal data, as summarized in Table 1.

The SCXRD data were collected on a Bruker SMART BREEZE diffractometer using graphite-monochromatized Mo K α radiation, $\lambda = 0.71073$ Å. Data reduction was carried out with SAINT,²⁶ and a multiscan absorption correction was performed with SADABS.²⁷ The crystal structure was solved by direct methods with SHELXS-97,²⁸ and the model was completed and optimized by refinement against $|F^2|$ using SHELXL-2014.²⁹ Energy-dispersive analysis by X-ray (EDAX) of the isolated blue crystals was carried out using a Hitachi S-3400N. EDX analyses under a similar process and reported elsewhere,^{30,31} which indicated that the peaks for Co and F in the

EDX analysis overlapped; however, the (Co + F):Te ratio was identified as 16.4:14.6, in agreement with the expected value (Figure S2).

IR spectra were recorded on an Agilent Cary 670-IR FTIR spectrometer in the spectral range of 400–4000 cm^{-1} , with an attenuated total reflection (ATR) accessory. The absence of hydrogen-bonded groups (absorption peak at approximately 3600 cm^{-1}) supported the fact that fluorine (rather than hydroxide) is part of the structure (Figure S4). UV/Vis/NIR absorption spectra were recorded using a Perkin-Elmer (USA) Lambda 950 UV-Vis-NIR spectrophotometer (Figure S5). X-ray photoelectron spectroscopy (XPS) measurements were performed using a Thermo Scientific K-Alpha⁺ instrument (Figure S7-S8). TGA was performed using a high-resolution TA Instruments Q50 Thermogravimetric Analyzer. Polycrystalline samples were put into alumina crucibles and heated at a rate of 10 $^{\circ}\text{C min}^{-1}$ from room temperature to 790 $^{\circ}\text{C}$ under flowing nitrogen gas (Figure S9).

The total thermal conductivity of polycrystalline samples was determined using the Hot Disk Thermal Constants Analyser (Model: TPS 2500S) in nitrogen. The DC magnetic susceptibility of **1** was measured using a Quantum Design Magnetic Properties Measurement System (MPMS). Zero-field-cooled (ZFC) and field-cooled (FC) data were collected in the temperature range 2–320 K under an external field of 200 Oe. The specific heat measurement was collected with the heat capacity option of a physical properties measurement system (PPMS-9, Quantum Design). Spin-polarized DFT calculations were carried out in the framework of the Vienna ab initio simulation package (VASP)³²⁻³⁴ using the projector augmented wave (PAW) method and the generalized gradient approximation of Perdew, Burke and Ernzerhof for the exchange-correlation functionals.³⁵ A plane wave cutoff energy of 400 eV and a threshold of self-consistent-field energy convergence of 10^{-6} eV were used with a set of $5 \times 5 \times 2$ k-points. To account for the strong electron correlation associated with the 3d states of Cobalt atoms, we employed the DFT plus on-site repulsion U (DFT+U) method as described by Dudarev³⁶. The electron localization function (ELF) has also been computed and allows the visualization of the nodal structure of the molecular orbital, including lone-pair electrons.³⁷ With the obtained electronic density and ELF, The Critic2 program^{38,39} with the Yu and Trinkle (YT) method⁴⁰ have used to determine the critical points of the ELF and to calculate the electronic charge and volume within the basins.

3. Results and discussion

3.1 Structural Descriptions

The crystal structure of **1** contains three distinct Co atoms and three Te atoms, which define the unusual 15:14 Co-to-Te stoichiometry in this phase. The location of the fluorine atom at Wyckoff site 6c (0, 0, z) is supported by its bond valence sum (BVS) value (in valence units)⁴¹ of -0.96 and by the IR results due to the absence of hydrogen-bonded groups (absorption peak at approximately 3600 cm^{-1} , see Figure S4). The BVS data for the Te (4.03–4.28) and Co (1.81–1.98) atoms confirm the valences of these metals to be IV and II, respectively. The coordination geometry around Co1 (site symmetry $\bar{1}$) is a slightly squashed octahedron composed of O atoms from six different tellurite anions (two each of Te1, Te2 and Te3) with two short [2.016 (5) Å] and four elongated [2.154 (5) and 2.165 (3) Å] bonds (Figure 1); the mean separation of 2.112 Å is similar to that observed in CoSeO₃ (2.143 Å).⁴² In contrast, Co2 is bonded to five O atoms [four with $d < 2.07$ Å and one with $d = 2.339$ (3) Å]. The value of 0.40 for the Addison τ parameter⁴³ for Co2 indicates a geometry intermediate between square-base pyramidal ($\tau = 0$) and trigonal bipyramidal ($\tau = 1$) but slightly closer to the former. The spread of bond lengths about Co2 is similar to those for the cobalt atom in LaBaCoO_{4.25} [1.999 (4)–2.335 (4) Å].⁴⁴ The Co3 cation in **1** is bonded to five O atoms and one F atom in a distorted octahedral geometry, with distances ranging from 2.040 (5) to 2.175 (4) Å and *cis* bond angles ranging from 77.66 (13) to 105.90 (13)°.

Te1 (site symmetry 3) has three O1 atoms as near neighbors with Te–O = 1.887 (3) Å and O–Te–O = 98.22 (13)°, defining a pyramidal shape, which is typical for this type of tellurium–oxygen grouping.⁴⁵ However, there are also three long Te–O interactions at 2.941 (4) Å [to O4], compared to the van der Waals separation for these atoms of 3.58 Å. We term this coordination geometry TeO₃₊₃.^{46,47} the calculated BVS for Te1 increases from 3.84 to 4.06 when considering all six O atoms. Te2 has three O atoms in close proximity ($d < 1.90$ Å) to form a more asymmetric trigonal pyramidal coordination environment with an O–Te–O bond angle distribution of 87.3 (2) – 94.67 (16)°. These three O atoms together with three distant O atoms [O4 at 2.655 (4) Å, O6 at 2.742 (4) Å and O6 at 2.850 (4) Å] make up a grossly distorted octahedron around Te2, again leading to a TeO₃₊₃ coordination geometry. The Te3 species has three O atoms as near neighbors in a trigonal pyramidal coordination environment, which is similar to the coordination environment observed in KY(TeO₃)₂.¹² The Te–O bond lengths range from 1.857 (3) to 1.891 (3) Å with a very narrow distribution of O–Te–O bond angles from 98.47 (15) to 98.97 (15)°.

The oxygen atoms in **1** adopt three kinds of coordinations: a) bonds to one Co and two Te in an essentially planar conformation (O1, O3, O5 and O7); b) bonds to one Te and three Co in distorted tetrahedral geometry (O2); c) bonds to three Te and one Co in a tetrahedral conformation (O4 and O6), where two long Te–O bonds are needed to form the distorted tetrahedral O(CoTe₃) unit. The unique fluorine atom is connected to three Co₃ atoms in an essentially planar configuration, hence acting as a bridging species to connect three CoO₅F octahedra. To the best of our knowledge, one fluoride anion usually bridges two transition metal cations, and the connection with three transition-metal cations is quite rare.

It should be mentioned that each Te₃ species together with Te1 and Te2 or two Te₂ species lead to a six-membered ring containing four long Te–O bonds around Te1/Te2 and two short Te–O bonds around Te₃ (Figure 2b). The O4⋯O6 distance of 2.826 (5) Å in the Te₃O₃ group is approximately equal to the long Te–O bonds around Te1/Te2, leading to the formation of a slightly distorted pentagonal face if these O4⋯O6 contacts are deemed to be “bonds”, in which case, the Te₃ species project out of the pentagonal face. A cluster of twelve of these pentagonal faces meet at 20 vertices [two Te1, six Te2, six O4 and six O6] to generate a distorted pyritohedral cavity (Figure 2a) centered at the point (0, 0, ½) and equivalent locations, where the two short Te₃–O bonds can be regarded as a “handle” fixed at the edge of O4⋯O6 “bond” (Figure 2c). Finally, the structural effect of the Te^{IV} lone pairs may be discussed, especially those on Te1 and Te2: if we assume that the lone pairs for these species occupy the fourth vertex of a tetrahedron, then the lone pairs and diagonal counterparts are all directed towards the point (0, 0, ½).

In fact, the electron localization function (reference) (ELF)³⁷ in the DFT (GGA-PBE) calculations allows visualization of the tellurium atom lone pairs, which are pointing as intuitively described above, as also seen in Figure S10. The calculated positions, distances to the corresponding Tellurium atom, volumes and charges of the electronic lone pairs are gathered in Table 2. The calculated Te–E distances range from 1.0720 to 1.1655 Å and are found slightly lower than in the oxotellurate(IV) compounds reported by Poupon *et al.*^{48,49} The calculated electronic charges are 2.93 *e*⁻, 3.04 *e*⁻ and 2.95 *e*⁻ for Te1, Te2 and Te3 lone pairs respectively. They fairly compares with the charges reported by Poupon *et al.* for which an example of a typical lone pair charge is 2.71 *e*⁻. The larger charges in our case are also associated to larger volumes around 20 Å (against ~15 Å in references 48 and 49). One should keep in mind that different codes with different approaches to represent the Kohn-Sham orbitals are used so the calculated values

are not strictly comparable with the literature. We focus on a qualitative analysis and compare the results of the lone pairs within the title phase. Here we note that the Te1-E distances is very similar with Te2-E distances, while is slightly higher than Te3-E distances. These results are consistent with different coordination environment of Te species (TeO_{3+3} for Te1 and Te2 ,while TeO_3 for Te3).

Then, the equator of the cavity is formed from a Te2-centered 6-membered ring, the hemisphere of the cavity is formed from a trio of Te3O_3 groups on the top or bottom, while the polar area of the cavity is formed from the Te1-centered groups (Figure 2a). More importantly, lone-pair self-containments, where extended tellurite networks are formed by themselves, are very rare. This novel way to accommodate Te(IV) lone-pair electrons need unusual Te-O bonds to form untypical polyhedrals, *i.e.*, the distorted square-based pyramids formed by less regular coordination found in BaTe_3O_7 ¹⁶ and the usual axial Te-O bond relative to the equatorial bonds found in BaTe_4O_9 .¹⁶ The coordination geometry TeO_{3+3} with a distorted octahedron shape in $\text{Co}_{15}\text{F}_2(\text{TeO}_3)_{14}$ supports this lone-pair self-contained configuration. In addition, there is a structure-directing effect on the position of the lone pair. One-dimensional lone-pair self-containment of barium tellurites is aided by large Ba^{2+} ions, resulting in lone-pair self-contained tellurite networks being isolated by one of two large Ba^{2+} , while zero-dimensional lone-pair self-containment in our sample results in a honeycomb-like Co-centered polyhedra network, where pyritohedron-shaped Te(IV) lone-pair cavities are finally sealed by trimeric octahedra joined by a common fluorine atom.

The extended structure of **1** features corner and edge sharing between the Co- and Te-centered polyhedra (Figure 1d). The infinite, honeycomb-like, layered structure may be schematically described in the stacking sequence. These sequences include a Co3/Te2-centered polyhedron layer, which is characterized by 12 rings of Co3 units and 6 rings of Te2 groups (details see Figure S11), a concomitant Co2/Te3-centered polyhedron layer attached at the top and bottom, followed by a Co1/Te1-centered polyhedron layer, and *another* Co2/Te3-centered polyhedron layer, where the former Co2/Te3 sheets are laterally displaced from each other by $x = 1/3$ and $y = 2/3$. Finally, *another* Co3/Te2-centered polyhedron layer is observed with displacement of $x = 1/3$ and $y = 2/3$ from the former ones. Finally, these honeycomb layers fused sequentially to form a continuous, three-dimensional structure, which encloses pyritohedron-shaped Te(IV) lone-pair self-contained

cavities. Due to rhombohedral crystal symmetry, there are no continuous channels of any significant size in this structure.⁴⁷

3.2 IR & UV-Vis Diffuse Reflectance Spectroscopy.

IR spectra reveal all the vibrations of Te-O and Co-O/F bonds (Figure S4). Multiple peaks situated in the region between 640 and 771 cm^{-1} are due to the Te-O vibrations.⁵⁰ The bands found at around 516 cm^{-1} may be attributable to the Co-O vibrations,⁵¹ associated with the cobalt ion located in octahedral holes. The bands observed at 455 and 478 cm^{-1} should be assigned to the $[\text{CoF}]^+$ cation. Compared with the single peak at $\sim 450 \text{ cm}^{-1}$ observed in CoF_2 ,⁵² the bands at 478 cm^{-1} are more likely to suggest fluorine-bridged structure, where the ionic contributions to the bonding are minimized.⁵³ Band gaps obtained from the (K/S) versus E plots for **I** (Figure S6) were found to be insulator ($E_g = 5.5 \text{ eV}$).

3.3 XPS Measurements.

The Co 2p XPS spectrum of **I** is shown on Figure S7. The binding energy value of 780.4 eV for the Co 2p_{3/2} is consistent with the data reported for Co(II) oxides compounds, such as CoO and Co(OH)₂,⁵⁴⁻⁵⁶ Furthermore, strong shake-up satellites observed at approximately 5 eV above the photo line is typical of high-spin Co²⁺.⁵⁷ However, the Co2p_{3/2} and Co2p_{1/2} energy separation of 16.0 eV which is 0.5 eV higher than observed in CoO,⁵⁸ is consistent with that of CoF₂,⁵⁴ indicating that Co cations are surrounded by mixed anions. The binding energy of the F 1s peak (Figure S8) centred at 683.8 eV is close to the values reported for transition metal fluorides, i.e CuF₂ (684.8 eV⁵⁹), FeF₂ (684.9 eV⁶⁰), MnF₂ (650.0 eV⁶¹), NiF₂ (650.1 eV⁶²), confirming the existence of bridging fluorine species in our samples.

3.4 DFT Calculations.

The GGA+U calculations were carried with the effective on-site repulsion $U_{\text{eff}} = U - J = 3-4 \text{ eV}$. For $U = 3 \text{ eV}$ and $U = 4 \text{ eV}$, the results are qualitatively similar, with topologies of the DOS

mainly conserved, and slightly increased band gap and magnetic moments are found only for $U=4$ eV. For the PDOS description, we focus on the calculations at $U=4$ eV.

To analyze the relationship between structure of transition metal parts and magnetic properties, we carried out DFT+U calculations on the title phase, leading to a semiconductor electronic structure even without inclusion of a Hubbard term U , *i.e.*, a band gap is opened with a value of 0.25 eV, while DFT may lead to erratic metallic states as far as d electrons are concerned. Within this approximation, the calculated magnetic moments on the different cobalt atoms, *i.e.*, the octahedral CoO_6 , the trigonal bipyramidal CoO_5 (TBP), and the heteroleptic (mixed anion) octahedral CoO_5F , are equal to 2.53 μB , 2.53 μB and 2.59 μB , respectively. These rather close values are consistent with a high-spin Co^{2+} (d^7) configuration on all the distinct Co sites despite the different environments and expected crystal field splitting, especially for TBP⁶³. For the latter, similar high-spin states of Co^{2+} have been described, for instance, in the $\text{Co}_2(\text{OH})\text{PO}_4$ or $\text{Co}_2(\text{OH})\text{AsO}_4$ phase.^{64,65} Then, applying a Hubbard term with $U=4$ eV led to a reasonable band gap of 2.75 eV (consistent with its blue color) and slightly increased magnetic moments of 2.76 μB , 2.74 μB and 2.77 μB with qualitatively similar characters of the electronic structure. We will focus on the results obtained using GGA+U ($U=4$ eV) for the rest of the discussion.

The projected density of states (PDOS) is represented in Figure 3, in which the upper part of the valence band and the conduction band are highlighted. For the $\text{TeO}_3(LP)$ entity, the contribution of the Te $5p$ states dominate the upper VB with a maximum of approximately -6.5 to -5 eV, while the Te $5s$ and $4d$ states are found to have a much smaller contribution in the whole range of the upper VB and are hybridized with O $2p$ states. The Te $5s$ and $4d$ states are found together with O $2p$ states in the CB. For the octahedral CoO_6 and CoO_5F_1 , the Co $3d$ up (\uparrow) spins are filled, while the down (\downarrow) spins are partially empty, leading to the probable configuration $(t_{2g})\uparrow^3 (e_g)\uparrow^2 (t_{2g})\downarrow^2 (e_g)\downarrow^0$. Similarly, CoO_5 , with spin (\uparrow) fully occupied and spin (\downarrow) partially empty, is also most likely in the Co^{2+} high spin state.

Focusing on the mixed anion CoO_5F_1 , it is interesting to analyze the different contributions of O^{2-} and F^- anions around cobalt. The $2p$ states of fluorine are found to have a higher contribution lower in the VB, while the O $2p$ states contribute more than F in the upper VB below the Fermi level, as expected for the more covalent character of the Co-O bond compared to Co-F.

3.5 Magnetic Properties

As shown in Figure 4, there is barely any difference between the ZFC and FC susceptibility data for **1** except for a small divergence below 20 K, possibly due to the magnetic anisotropy of the Co^{2+} ion. In the high-temperature paramagnetic region, the magnetic susceptibility approximated to M/H could be fitted by a Curie–Weiss law $\chi(T) = C/(T - \theta_{CW}) + \chi_o$, where C is the molar Curie constant and θ_{CW} is the Curie–Weiss temperature. The χ_o term contains temperature-independent contributions stemming from the diamagnetism of the core electron shells and the van Vleck paramagnetism of the Co^{2+} ions. The best-fit values of Curie–Weiss law are $C = 3.33$ (1) $\text{mol}^{-1}\cdot\text{K}$, $\theta_{CW} = -63.7$ (2) K and $\chi_o = 0.014$ (1) $\text{emu/mol}\cdot\text{Oe}\cdot\text{Co}$. The effective magnetic moment is $\mu_{\text{eff}} = 5.15$ (2) μ_{B} per Co^{2+} ion: this value is considerably larger than the spin-only value (3.87 μ_{B}) expected for high-spin (HS) $d^7 \text{Co}^{2+}$ ($S = 3/2$) ions, which implies a significant orbital contribution for the magnetically anisotropic Co^{2+} ions. The negative value of θ_{CW} suggests the presence of dominant antiferromagnetic exchange interactions J . Using the mean-field (MF) formula, we may evaluate J from the Curie–Weiss temperature: $\theta_{CW} = zJS(S + 1)/3k_B$, where z is the number of the nearest neighbor Co^{2+} spins and k_B is the Boltzmann constant. Here, we take the average value of $z = 5.6$, based on the fact that Co1 has six nearest neighbors, Co2 has five nearest neighbors, and Co3 has six nearest neighbors. This yields $J_{MF}/k_B \approx -9.1$ K for $S = 3/2$. The sizable antiferromagnetic exchange interactions are further justified by considering the bond angles between the Co^{2+} ions. The average Co–O–Co bond angle is 105.1° , beyond the range in which ferromagnetic exchange interactions are dominant ($90\text{--}100^\circ$).⁶⁶ Moreover, as the Co–F–Co bond angle is 118.2 (1) $^\circ$, the intermediate strength of the antiferromagnetic coupling is in accordance with the Goodenough–Kanamori–Anderson superexchange rules, which predict that antiferromagnetic interactions become stronger as the bond angles mediating superexchange paths increase towards 180° beyond the crossover angle where the exchange interaction changes its sign from ferromagnetic to antiferromagnetic.

At low temperatures, $\chi(T)$ displays a small kink and a subsequent drop towards zero kelvin, giving an indication of antiferromagnetic ordering. The transition temperature was determined to be $T_N = 9.6$ K by a sharp peak in the derivative of $d(\chi T)/dT$, as plotted in the inset of Figure 4a. λ -type anomalies are also found in the heat capacity of the title phase at temperatures matching well with those where characteristic susceptibility features were determined (see Figure 4c).

From the ratio $f = |J_{MF}/T_N| \sim 1.2$ (1), we infer that **1** has a three-dimensional magnetic structure . The plot of magnetization *versus* applied field at 2 K is shown in Figure 4b. The magnetization increases linearly up to 4.5 T without detectable hysteresis and subsequently exhibits a steep increase. The former feature is fully consistent with an antiferromagnetic (rather than weakly ferrimagnetic) system, and the latter may be due to a spin-flop transition at $H_{SF} = 4.5$ T.

3.6 Thermal Conductivity

In order to see the effect of rattling of Te atoms with lone pair electrons on physical properties, we measured total thermal conductivity (κ) for **1**, the result of which is plotted in Figure 5. κ includes two parts of electronic thermal conductivity (κ_e) and lattice thermal conductivity (κ_L). According to the Wiedemann–Franz law, $\kappa_e = LT/\rho$, here L represents the Lorenz number and ρ is the electrical resistivity. The electronic contribution of thermal conductivity is inversely proportional to electrical resistivity. As **1** is insulator, ρ is inclined to infinite. Thus κ_e is approximately zero. The total thermal conductivity is approximately equal to κ_L . κ_L of **1** at room temperature is estimated to be 0.18 W/(Km) (more clear see Figure S12). The value is lower than that of well-known high performance thermoelectric materials such as PbTe (~1.5~2.0 W/mK at T=300 K),^{67,68} Bi₂Te₃ (~0.6~0.9 W/mK at T=300 K),⁶⁹ Mg₃Sb₂ (~0.80~1.40 W/mK at T=300 K),⁷⁰ SnSe (~0.62 W/mK at RT),⁷¹ β -Zn₄Sb₃ (~0.65 at RT),⁷² and tetrahedrites (~0.40~0.50 at RT).⁷³ The data are even comparable with the lowest κ_L at high temperature, for example SnSe (~0.30 W/mK at T=700 K),⁷¹ and nano Bi_xSb_{2-x}Te₃ (~0.24 W/mK at T=550 K).⁶⁹ Note that κ_L is determined by the independent parameters, for examples, specific heat, group velocity, and mean free path of phonons/relaxation time, etc. Thus minimizing κ_L is an inherent method for developing highly efficient thermoelectric materials, as proposed by Slack.⁷⁴ So-called “phonon-glass and electron-crystal” materials with a low κ_L , such as skutterudites⁷⁵ and clathrates⁷⁶ was found to contain caged structures, where guest atoms vibrates with large amplitude in oversized atomic cages, so-called rattling, which can scatter heat carrying phonons. More recently, rattling-like local vibration in a cation with lone pair electrons was also found to lower κ_L .^{77,78}

Therefore, the lower κ_L value of **1** seems to be correlated with the large oscillation amplitude of the Te atoms with lone pair electrons leading to rattling motions, similar to heavy Bi atoms with lone pair electrons in $\text{LaOBiS}_{2-x}\text{Se}_x$.⁷⁸ The lower κ_L value corresponds to the lower rattling energy. Compared with the narrow distance between double layers of $\text{Bi}(\text{S,Se})_5$ -lattice structure in $\text{LaOBiS}_{2-x}\text{Se}_x$,⁷⁸ where the lone pairs on the Bi^{3+} point toward the interior of the layers. Pyritohedron-shaped Te^{IV} lone-pair self-contained cavities in **1** provided a much larger free space allowing Te atom to vibrate with large amplitude, which leads to lower κ_L . However, the detailed origin of the lower κ_L needs inelastic neutron scattering techniques to investigate phonons of **1**.

4. Conclusion

In conclusion, $\text{Co}_{15}\text{F}_2(\text{TeO}_3)_{14}$ was obtained by optimized hydrothermal synthesis, including a complex mineralization process, and features a unique structural solution to accommodate Te^{IV} lone pairs in pyritohedron-shaped closed cavities. This special framework provides a much larger free space allowing Te atoms to vibrate with large amplitude, which leads to extremely low lattice thermal conductivity. The magnetic structure is an $S=3/2$ honeycomb-like spin network.

Supporting Information

Calculated and observed powder X-ray diffraction patterns for $\text{Co}_{15}\text{F}_2(\text{TeO}_3)_{14}$, EDX, IR, TGA, UV/Vis/NIR, XPS, and BVS are provided as Supporting Information. Deposition number CCDC 1867643 for $\text{Co}_{15}\text{F}_2(\text{TeO}_3)_{14}$. This material is available free of charge via the Internet at <http://pubs.acs.org>.

AUTHOR INFORMATION

Corresponding Author

m.f.lv@hotmail.com (Minfeng Lü)

ORCID[®]

Minfeng Lü: 0000-0003-2576-3840

Notes

The authors declare no competing financial interests.

Acknowledgments

M. L., J. J., B.Z., Y. Z., T. Z., H. Y., and Y. J. acknowledge support from the National Natural Science Foundation of China (Award No. 21671185). The regional computational cluster supported by Lille University, CPER Nord-Pas-de-Calais/CRDER, France Grille CNRS and FEDER is thanked for providing computational resources.

References

- 1 H. Kageyama, K. Hayashi, K. Maeda, J. P. Attfield, Z. Hiroi, J. M. Rondinelli, K. R. Poeppelmeier, *Nat. Commun.*, 2018, **9**, 772.
- 2 Y. Kamihara, T. Watanabe, M. Hirano, H. Hosono, *J. Am. Chem. Soc.*, 2008, **130**, 3296–3297.
- 3 M. Al-Mamouri, P. P. Edwards, C. Greaves, M. Slaski, *Nature*, 1994, **369**, 382–384.
- 4 Y.-I. Kim, P. M. Woodward, K. Z. Baba-Kishi, C. W. Tai, *Chem. Mater.*, 2004, **16**, 1267–1276.
- 5 Y. Kobayashi, O. J. Hernandez, T. Sakaguchi, T. Yajima, T. Roisnel, Y. Tsujimoto, M. Morita, Y. Noda, Y. Mogami, A. Kitada, M. Ohkura, S. Hosokawa, Z. Li, K. Hayashi, Y. Kusano, J. e. Kim, N. Tsuji, A. Fujiwara, Y. Matsushita, K. Yoshimura, K. Takegoshi, M. Inoue, M. Takano and H. Kageyama, *Nat. Mater.*, 2012, **11**, 507–511.
- 6 S. Muhammady, Y. Kurniawan, S. Ishiwata, A. Rousuli, T. Nagasaki, S. Nakamura, H. Sato, A. Higashiya, A. Yamasaki, Y. Hara, A. Rusydi, K. Takase, Y. Darma, *Inorg. Chem.*, 2018, **57**, 10214–10223.
- 7 J.-B. Labégorre, R. Al Rahal Al Orabi, A. Virfeu, J. Gamon, P. Barboux, L. Pautrot-d'Alençon, T. Le Mercier, D. Berthebaud, A. Maignan, E. Guilmeau, *Chem. Mater.*, 2018, **30**, 1085–1094.
- 8 U. Opik, M. H. L. Pryce, *Proc. R. Soc. London, Ser. A* 1957, **238**, 425–447.
- 9 R. G. Pearson, *J. Am. Chem. Soc.*, 1969, **91**, 4947–4955.
- 10 H. Zhang, M. Zhang, S. Pan, X. Dong, Z. Yang, X. Hou, Z. Wang, K. B. Chang, K. R. Poeppelmeier, *J. Am. Chem. Soc.* 2015, **137**, 8360–8363.
- 11 J.-G. Mao, H.-L. Jiang, F. Kong, *Inorg. Chem.*, 2008, **47**, 8498–8510.
- 12 Y. Kim, D. W. Lee, K. M. Ok, *Inorg. Chem.*, 2015, **54**, 389–395.
- 13 M. Johnsson, K. W. Törnroos, P. Lemmens, P. Millet, *Chem. Mater.*, 2003, **15**, 68–73.

- 14 M. Dutreilh, P. Thomas, J.-C. Champarnaud-Mesjard, B. Frit, *Solid State Sci.*, 2001, **3**, 423–431.
- 15 Y.-G. Chen, N. Yang, X.-N. Yao, C.-B. Li, Y. Guo, X.-M. Zhang *Inorg. Chem.*, 2018, DOI: 10.1021/acs.inorgchem.8b00266.
- 16 M. G. Johnston, W. T. A. Harrison, *J. Am. Chem. Soc.*, 2002, **124**, 4576–4577.
- 17 S. Hu, M. Johnsson, J. M. Law, J. L. Bettis, M.-H. Whangbo, R. K Kremer, *Inorg. Chem.*, 2014, **53**, 4250–4256.
- 18 M. Pregelj, O. Zaharko, A. Zorko, Z. Kutnjak, P. Jeglic, B. P. Brown, Z. Jagodic, H. Berger, D. Arcon, *Phys. Rev. Lett.*, 2009, **103**, 147202(4).
- 19 M. Johnsson, K. W. Törnroos, F. Mila, P. Millet, *Chem. Mater.*, 2000, **12**, 2853–2857.
- 20 R. Becker, M. Johnsson, R. K. Kremer, H.-H. Klauss, P. Lemmens, *J. Am. Chem. Soc.*, 2006, **128**, 15469–15475.
- 21 R. Takagi, M. Johnsson, V. Gnezdilov, R. K. Kremer, W. Brenig, P. Lemmens, *Phys. Rev. B* 2006, **74**, 0144131–0144138.
- 22 D. Zhang, M. Johnsson, H. Berger, R. K. Kremer, D. Wulferding, P. Lemmens, *Inorg. Chem.*, 2009, **48**, 6599–6603.
- 23 J. P. Laval, N. J. Boukharrata, *Acta Crystallogr.*, 2009, **C65**, i1.
- 24 J. P. Laval, N. J. Boukharrata, P. Thomas, *Acta Crystallogr.* 2008, **C64**, i12.
- 25 S. Hu, M. Johnsson, *Dalton Trans.*, 2012, **41**, 12786–12789.
- 26 *SAINT: Area-Detector Integration Software*; Siemens Industrial Automation, Inc.: Madison, 1996.
- 27 *SADABS: Area-Detector Absorption Correction*; Siemens Industrial Automation, Inc.: Madison, 1995.
- 28 G. M. Sheldrick, *Acta Cryst.*, 2008, **A64**, 112–122.
- 29 G. M. Sheldrick, *Acta Cryst.*, 2015, **C71**, 3–8.
- 30 H.B. Yahia, M. Shikano, H. Kobayashi, *Dalton Trans.*, 2013, **42**, 7158–7166.
- 31 S. S. Fedotov, N.R. Khasanova, A. S. Samarin, O. A. Drozhzhin, D. Batuk, O. M. Karakulina, J. Hadermann, A. M. Abakumov, E. V. Antipov, *Chem. Mater.*, 2016, **28**, 411–415.
- 32 G. Kresse, J. Hafner, *Phys. Rev. B*, 1993, **47**, 558.
- 33 G. Kresse, J. Furthmüller, *Comput. Mater. Sci.*, 1996, **6**, 15.
- 34 G. Kresse, J. Furthmüller, *Phys. Rev. B*, 1996, **54**, 11169.
- 35 J. P. Perdew, K. Burke, M. Ernzerhof, *Phys. Rev. Lett.*, 1996, **77**, 3865.
- 36 S. L. Dudarev, G. A. Botton, S. Y. Savrasov, C. J. Humphreys, A. P. Sutton, *Phys. Rev. B*, 1998, **57**, 1505.
- 37 B. Silvi, A. Savin, *Nature* 1994, **371**, 683–686.
- 38 A. Otero-de-la-Roza, E. R. Johnson and V. Luaña, *Comput. Phys. Commun.*, 2014, **185**, 1007–1018.
- 39 A. Otero-de-la-Roza, M. A. Blanco, A. Martín Pendás and V. Luaña, *Comput. Phys. Commun.*, 2009, **180**, 157–166.
- 40 M. Yu, D. R. Trinkle, *J. Chem. Phys.*, 2011, **134**, 064111.
- 41 N. E. Brese, M. O’Keeffe, *Acta Crystallogr.*, 1991, **B47**, 192–197.
- 42 K. Kohn, K. Inoue, O. Horie, S. I. Akimoto. *J. Solid State Chem.*, 1976, **18**, 27–37.
- 43 A. W. Addison, N. T. Rao, J. Reedijk, J. van Rijn, G. C. Verschoor, *J. Chem. Soc., Dalton Trans.*, 1984, 1349–0000.
- 44 J. Seddon, E. Suard, M. A. Hayward, *J. Am. Chem. Soc.*, 2010, **132**, 2802–2810.

- 45 D. W. Lee, D.-b. Bak, S. B. Kim, J. Kim, K. M. Ok, *Inorg. Chem.*, 2012, **51**, 7844–7850.
- 46 I. D. Brown, *J. Solid State Chem.*, 1974, **11**, 214–233.
- 47 J. T. S. Irvine, M. G. Johnston, W. T. A. Harrison, *Dalton Trans.*, 2003, 2641–2645.
- 48 M. Poupon, N. Barrier, S. Petit, S. Boudin. *Dalton Trans.*, 2017, **46**, 1927-1935.
- 49 M. Poupon, N. Barrier, S. Petit, S. Clevers, V. Dupray. *Inorg. Chem.*, 2015, **54**, 5660-5670.
- 50 S.-W. Bae, C.-Y. Kim, D. W. Lee, K. M. Ok, *Inorg. Chem.*, 2014, **53**, 11328-11334.
- 51 C.-W. Tang, C.-B. Wang, S.-H. Chien, *Thermochim. Acta*, 2008, **473**, 68–73.
- 52 M. Balkanski, P. Moch, G. Parisot, *J. Chem. Phys.*, 1966, **44**, 940.
- 53 B. Frlec, D. Gantar, J. H. Holloway, *J. Fluorine Chem.*, 1982, **19**, 485-500.
- 54 D. C. Frost, C. A. McDowell, I. S. Woolsey, *Molecular Physics.*, 1974, **27**, 1473-1489.
- 55 J. Haber, L. Ungier, *J. Electron Spectrosc. Relat. Phenom.*, 1977, **12**, 305.
- 56 N. S. McIntyre, M. G. Cook, *Anal. Chem.*, 1975, **47**, 2208.
- 57 D. Barreca, C. Massignan, S. Daolio, M. Fabrizio, C. Piccirillo, L. Armelao, E. Tondello, *Chem. Mater.*, 2001, **13**, 588.
- 58 B. J. Tan, K. J. Klabunde, P. M. A. Sherwood, *J. Am. Chem. Soc.*, 1991, **113**, 855-861.
- 59 R.P. Vasquez, *Surf. Sci. Spectra*, 1993, **2**, 155.
- 60 M. Kasrai, D.S. Urch, *J. Chem. Soc. Faraday Trans. II*, 1979, **75**, 1522.
- 61 A. Aoki, *Jpn. J. Appl. Phys.*, 1976, **15**, 305.
- 62 S.W. Gaarenstroom, N. Winograd, *J. Chem. Phys.*, 1977, **67**, 3500.
- 63 A. E. Smith, H. Mizoguchi, K. Delaney, N. A. Spaldin, A. W. Sleight, M. A. Subramanian, *J. Am. Chem. Soc.*, 2009, **131**, 17084–17086.
- 64 M. E. Foglio, G.E. Barberis, *Braz. J. Phys.*, 2006, **36(1A)**, 40-54.
- 65 J. M. Rojo, J. R. Fernández, M.T. Fernández-Díaz, T. Rojo, *Phys. Rev. B*, 2010, **81**, 134431.
- 66 M. Du, Y.-M. Guo, X.-H. Bu, J. Ribas, *Eur. J. Inorg. Chem.*, 2004, 3228-3231.
- 67 Y. Pei, A. LaLonde, S. Iwanaga, G.J. Snyder, *Energy Environ Sci.*, 2011, **4**, 2085.
- 68 A. LaLonde, Y. Pei, G. J. Snyder, *Energy Environ Sci.*, 2011, **4**, 2090.
- 69 B. Poudel, Q. Hao, Y. Ma, Y. Lan, A. Minnich, B. Yu, X. Yan, D. Wang, A. Muto, D. Vashaee, X. Chen, J. Liu, M. S. Dresselhaus, G. Chen, Z. Ren, *Science*, 2008, **320**, 634.
- 70 H. Tamaki, H. K. Sato, T. Kanno, *Adv. Mater.*, 2016, **28**, 10182.
- 71 L.-D. Zhao, S.-H. Lo, Y. Zhang, H. Sun, G. Tan, C. Uher, C. Wolverton, V. P. Dravid, M. G. Kanatzidis, *Nature*, 2014, **508**, 373.
- 72 T. Caillat, J.-P. Fleurial, A. Borshchevsky, *J. Phys. Chem. Solids*, 1997, **58**, 1119.
- 73 K. Suekuni, K. Tsuruta, M. Kunii, H. Nishiata, E. Nishibori, S. Maki, M. Ohta, A. Yamamoto, M. Koyano, *J. Appl. Phys.*, 2013, **113**, 043712.
- 74 G. A. Slack, *CRC Handbook of Thermoelectrics*, (Ed: D. M. Rowe), CRC Press, Boca Raton, FL, USA 1995, 407.
- 75 G. S. Nolas, D. T. Morelli, T. M. Tritt, *Annu. Rev. Mater. Sci.*, 1999, **29**, 89.
- 76 T. Takabatake, K. Suekuni, T. Nakayama, E. Kaneshita, *Rev. Mod. Phys.*, 2014, **86**, 669.
- 77 K. Suekuni, C. H. Lee, H. I. Tanaka, E. Nishibori, A. Nakamura, H. Kasai, H. Mori, H. Usui, M. Ochi, T. Hasegawa, M. Nakamura, S. Ohira-Kawamura, T. Kikuchi, K. Kaneko, H.

Nishiata, K. Hashikuni, Y. Kosaka, K. Kuroki, T. Takabatake, *Adv. Mater.*, 2018, **30**, 1706230.

78 C. H.Lee, A. Nishida, T. Hasegawa, H. Nishiata, H. Kunioka, S. Ohira-Kawamura, M. Nakamura, K. Nakajima, Y. Mizuguchi, *Appl. Phys. Lett.*, 2018, **112**, 023903.

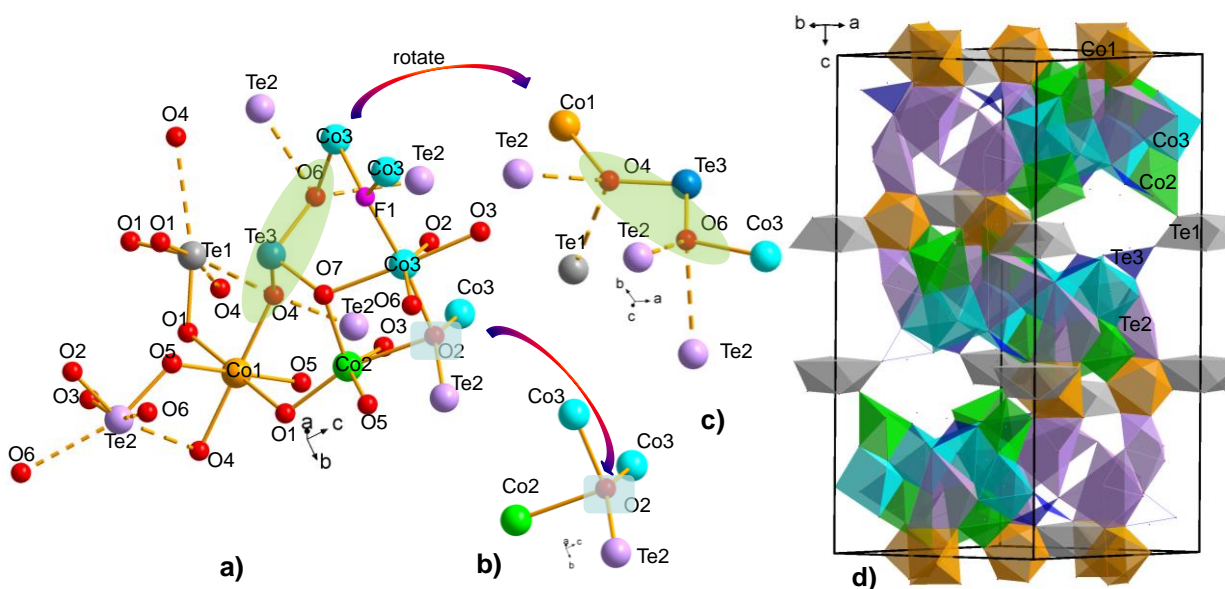


Figure 1: a) View of a fragment of the crystal structure of **1** showing the cation coordination environments and atom labeling. The long Te–O bonds are shown as dashed lines (see text); b) detail of the O2 coordination environment; c) detail of the O6 coordination environment. d) Projection of the structure of **1** along the [110] direction.

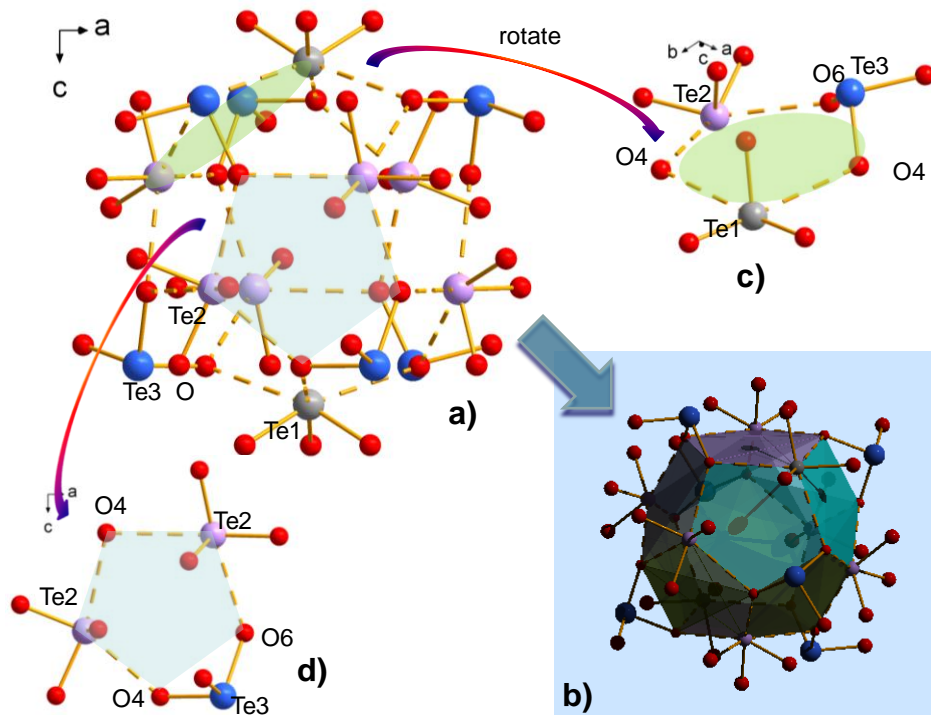


Figure 2: a) View down [010] of a $[(\text{TeO}_3)_{14}]^{28-}$ building unit, which encloses a pyritohedral cavity [highlighted in b)] made up of twelve distorted pentagonal faces (one shaded light blue), each of which is formed from a trio of TeO_3 groups (green circle); c) expanded view of a trio of TeO_3 groups; d) expanded view of the pentagonal face $\text{Te}_2/\text{O}_4/\text{Te}_2/\text{O}_6/\text{O}_4$ with an $\text{O}_4 \cdots \text{O}_6$ as one edge and the Te_3 atom as a “handle”. The lone pairs of the Te_1 and Te_2 atoms point into the cavity, which has atom-to-atom dimensions of $\sim 4.3 \text{ \AA} \times \sim 4.3 \text{ \AA}$.

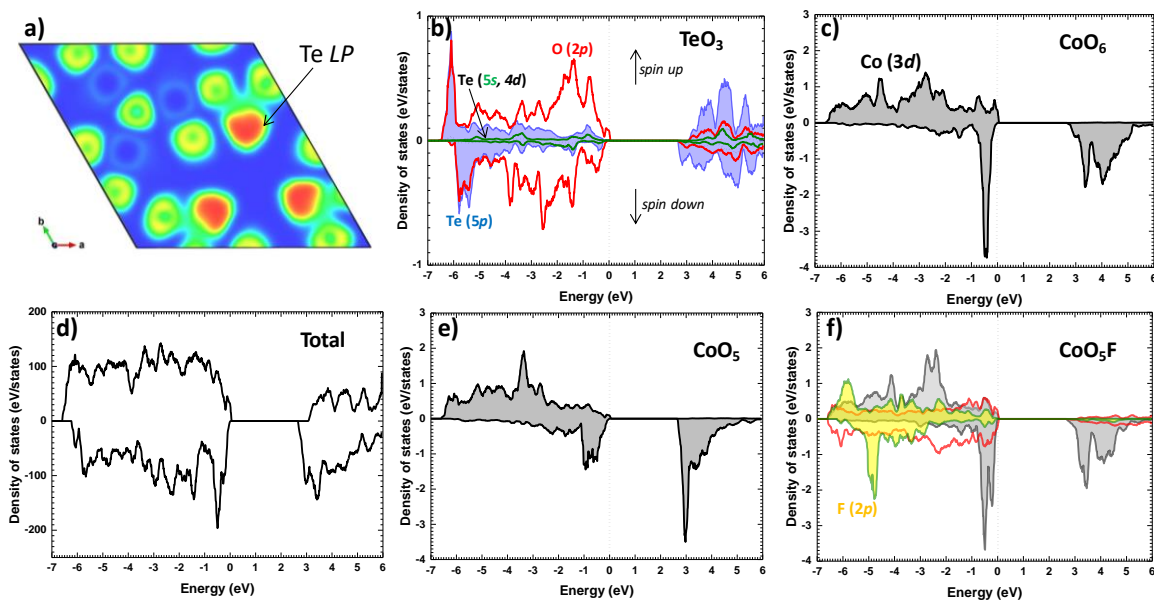


Figure 3. a) Slice of the DFT calculated valence electron localization function (ELF) for $\text{Co}_{15}\text{F}_2(\text{TeO}_3)_{14}$ with blue corresponding to weak localization and orange to complete localization (lone pairs). Projected density of states (PDOS) focusing on TeO_3 (b), CoO_6 (c), CoO_5 (e), CoO_5F entities and total density of states (f).

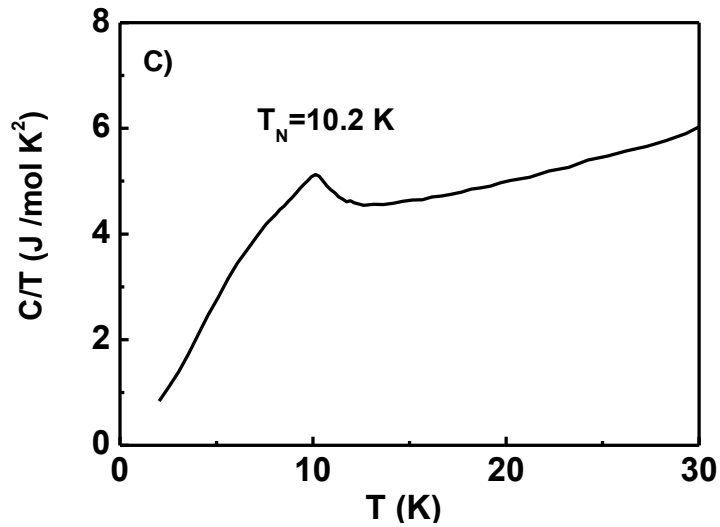
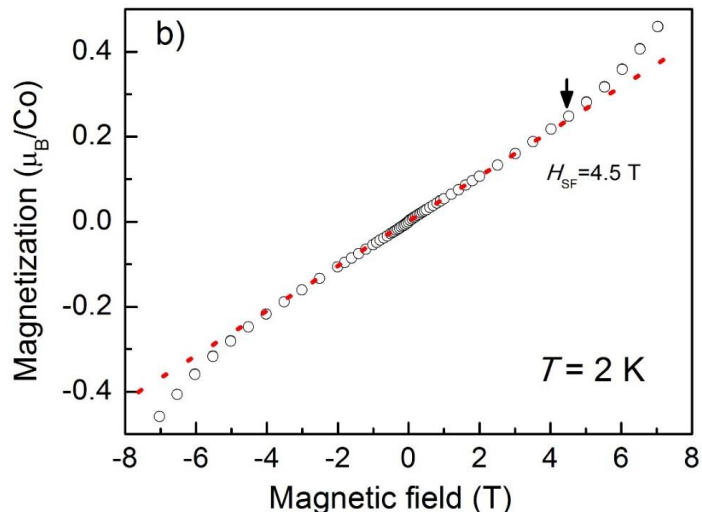
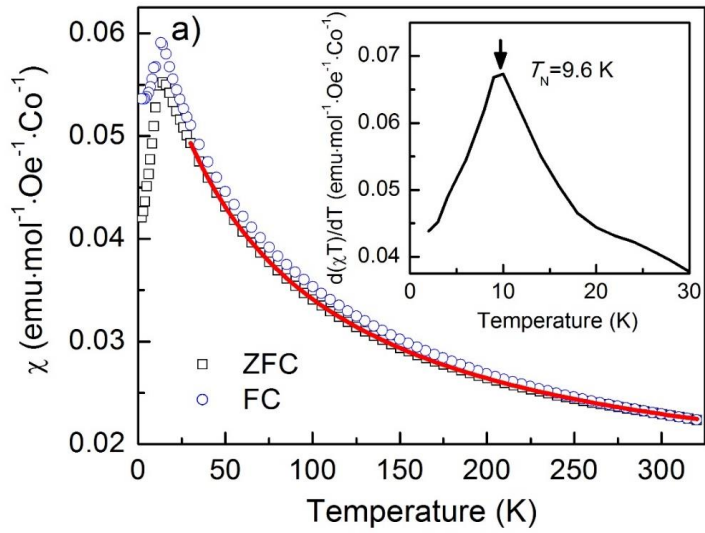


Figure 4: (a) The magnetic susceptibility of **1** measured under an external field of $H = 200$ Oe in the temperature range of 2–320 K. The solid line is a Cuire–Weiss fit. The inset shows the derivative of $\chi(T)$ versus T at low temperatures, indicating the onset of antiferromagnetic ordering at $T_N = 9.6$ K. (b) Magnetization isotherm measured at $T = 2$ K. The dashed line is a fit to a linear dependence of the magnetization; the arrow indicates the onset of the proposed ‘spin-flop’ transition. (c) Specific heat of $\text{Co}_{15}\text{F}_2(\text{TeO}_3)_{14}$.

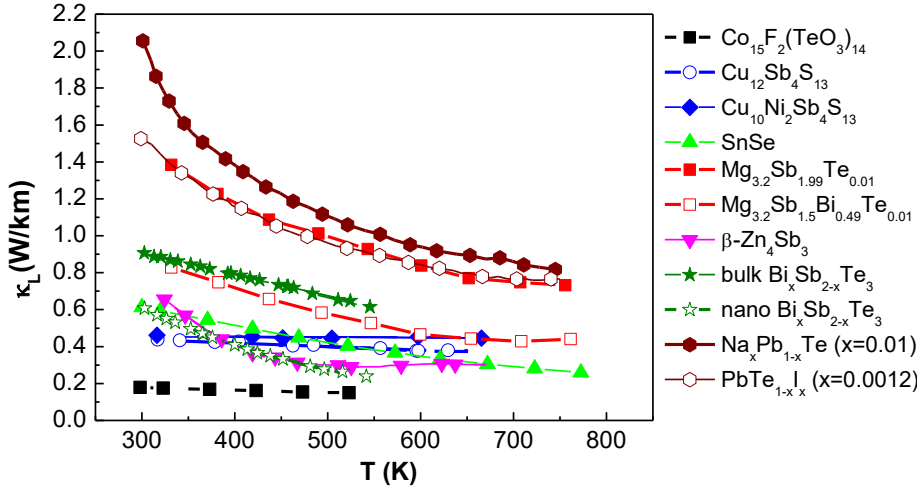


Figure 5: Lattice thermal conductivity as a function of temperature for $\text{Co}_{15}\text{F}_2(\text{TeO}_3)_{14}$ and state-of-the-art thermoelectric materials.

Table 1. Crystal data, measurement parameters and structural refinement parameters of $\text{Co}_{15}\text{F}_2\text{O}_4\text{Te}_{14}$ at room temperature.

	$\text{CsMn}_3\text{F}_6(\text{SeO}_3)_2$
Molar weight (g/mol)	3380.35
Symmetry	trigonal
Space group	$R\bar{3}$
a (Å)	11.6649 (4)
c (Å)	27.3173 (10)
V (Å ³)	219.1 (3)
μ (mm ⁻¹)	15.084
R(int) (%)	2.55
indep all ($I > 2\sigma(I)$)	1776
indep obsd ($I > 2\sigma(I)$)	1665
Number of refined	113
$R(F)^a [I > 2\sigma(I)/\text{all data, \%}]$	2.23/2.52

$$R_w (F^2)^b [I > 2\sigma(I)/\text{all data, } 4.45/4.53$$

$${}^a R = \sum \| |F_o| - |F_c| \| / \sum |F_o|, {}^b R_w = [\sum w(|F_o|^2 - |F_c|^2)^2 / \sum w|F_o|^2]^{1/2}$$

Table 2. Description of the Lone Pairs: positions, Te-E distances, charges and volumes.

Electronic lone pair	Position (x, y, z)	Distance to Te (Å)	Charge (e ⁻)	Volume (Å ³)
E1 (Te1)	0 0 0.6000	1.1655	2.93	20.8
E2 (Te2)	0.1875 0.75 0.2000	1.1651	3.04	21.3
E3 (Te3)	0.75 0.862 0.0278	1.0720	2.95	20.3

